Non-destructive corrosion inspection of reinforced concrete structures using an autonomous flying robot

P. Pfändler [a,*], K. Bodie [b], G. Crotta [b], M. Pantic [b], R. Siegwart [b], U. Angst [a]

[a] *Institute for Building Materials, ETH Zurich, Zurich, Switzerland*
[b] *Institute of Robotics and Intelligent Systems, ETH Zurich, Zurich, Switzerland*

ABSTRACT

Autonomous non-destructive testing (NDT) on reinforced concrete structures has a large potential to overcome the limitations of current routine inspection techniques, often not capable of detecting corrosion at an early stage. Here, the development and validation of two probes, tailored to acquire contact-based NDT data with the help of a hexacopter, is presented. Each probe allows the combined measurement of two essential parameters in the condition assessment: half-cell potentials and concrete electrical resistivity. Strategies are presented to monitor probe functionality during operation and detect loss of contact between probe and structure, which is considered essential for autonomous NDT. The presented approach enables effective and reliable autonomous corrosion inspection, surpassing traditional visual inspections by localizing corrosion at an early stage, allowing engineers a better planning of maintenance. The successful application in a concrete bridge inspection sets the stage for future research in autonomous inspections with robots in various fields of applications.

1. Introduction

Most civil infrastructure is built with reinforced concrete (RC) [1]. Although the material is generally durable, the corrosion of embedded reinforcing steel is among the most frequent causes of premature degradation [2,3]. An analysis of road repair costs in Switzerland highlighted that, on average, 50% of the maintenance and repair costs directly result from corrosion-related damages [2]. The aging of the infrastructure will lead to an increased need for inspections in the coming decades [4], especially bridges.

The purpose of the inspection is to help infrastructure owners make decisions about interventions to extend the service life of the structure while considering the condition of the structure and limited financial resources. However, the current practice of assessing the corrosion condition, especially with non-destructive testing (NDT) methods, is limited in terms of efficiency and costs. One reason is that certain structural parts are hardly accessible for inspectors without additional specialized equipment (e.g., lifting platforms, special trucks for mobile bridge inspections, etc.) to conduct NDT measurements. NDT measurements often require physical contact with the concrete surface (e.g., ground penetrating radars, eddy current). As a result of these factors, high personnel involvement leads to high inspection costs. Furthermore,

road closings are inevitable under certain circumstances, reducing the network availability for the end-users, or inspections must be executed during night shifts. Due to these drawbacks, only visual inspections are performed at regular time intervals on structures. A limitation of visual inspection is that only certain types of damage can be detected, such as rust stains, cracks, or concrete spalling. However, in the case of chloride-induced corrosion, a significant amount of cross-sectional loss of the reinforcing steel can occur without visible traces on the concrete surface [5]. An extreme case of this behavior was a bridge collapse in Wales without warning [6] due to chloride-induced corrosion. Even though the bridge was regularly inspected, no signs of deterioration were reported [7]. In conclusion, a purely visual inspection might not reveal early and relevant damages to the steel reinforcement and thus limit the possibility of operating the large stock of structures safely and economically, especially if structures are exposed to chlorides. Sole reliance on visual inspections is thus inadequate.

The inspection of RC structures can be split into three main types: visual, NDT, and destructive testing. Each offers ideally the possibility of increasing informative value but also increases the inspection costs. NDT methods allow the characterization of material properties [8]. The literature describes and summarizes numerous applications of NDT methods for bridges [9].

For example, half-cell potential (HCP) mapping is a technique that allows the non-destructive localization of chloride-induced corrosion on RC structures. The technology is well-known and is standardized in several guidelines [10–14]. The working principle is that a reference electrode (RE) is positioned at different locations on the concrete surface. A high input impedance voltmeter measures the potential difference to the reinforcing steel. Passive and corroding parts of the reinforcement show different potentials. Typically, the RE is positioned on predefined marks by the inspectors (e.g., by chalk), forming a grid between 15 and 50 cm. Often, several thousand points are acquired for a complete surface scan. Potential data from large structures are usually collected with wheel electrodes (single or with an array of two or more wheeled electrodes) for flat surfaces [15]. This high density of measurement points over a large surface area results in high inspection costs, especially on hardly accessible structural parts.

Efforts to automate RC structure assessments have led to the development of various types of robots. These state-of-the-art approaches differ in their selection of NDT methods, the method of locomotion (vortex, wheels, air pads, etc.), and the type of navigation. Locomotion limitations can reduce the application area to certain structural parts [16–20]. For example, wheeled robots, which are limited to inspecting horizontally flat surfaces (e.g., bridge decks) with several NDT methods, are described in [21,22]. For locations that are difficult to access, other forms of propulsion were used in which the robotic platform stays in contact with the concrete surface [23–26]. However, these robots might be limited to applications where the robot remains on a continuously smooth surface and must be manually moved around a corner (e.g., from a column to the underside of a bridge).

Unmanned aerial vehicles (UAV) for inspection tasks are gaining momentum. The development of such UAVs for visual inspections has already resulted in cost savings of about 60% for visual inspections of bridges in 2016 [27], since they are able to access remote structural locations quickly and without the need for large supporting equipment or lane closures. Furthermore, the first automatic image processing algorithms demonstrated the capability of detecting surface damages, such as cracks, in real-time with high accuracy [28]. With the increase in developments of artificial intelligence (AI), crack detection on images is being partially replaced by convolutional neural networks, as shown in [29]. Despite their advantages, common UAVs do not have the capability to physically interact with the environment while maintaining stable flight. A controlled physical interaction with the structure would allow the application of the HCP mapping to reliably detect localized corrosion or enable the use of other NDT equipment.

The first attempts to establish physical contact between UAVs and a structure were made after 2015 [19,20]. The main challenges identified were high energy consumption, which resulted in limited flight time, possible legal issues with handling drones safely, and the limited payload, which in turn restricted the number of NDT sensors on the platform in these studies. Despite these challenges, the opportunities offered in inspection and maintenance are highly acknowledged [16,18–20].

In order to exploit the potential of the UAVs with standard and well-established NDT methods, a flying inspection robot was developed in the present work to autonomously conduct potential mapping on RC structures. The flying robot was equipped with a sensor for HCP mapping and measuring concrete resistivity. This paper. It also highlights the advantages of corrosion inspection with flying robots and presents the first results obtained from laboratory flights and engineering structures.

2. Methods and materials

This section is organized into six subsections. The first provides a succinct description of the omnidirectional flying platform. The second part introduces the two NDT sensors (point sensor and combined rolling sensor), specifically designed for integration with the flying platform and autonomous inspection flights. The mortar specimens used to validate the robotic platform and the sensor are described in the third part. The subsequent subsection presents the conversion process from resistance to resistivity for the two sensors. The fifth subsection presents the seven individual experiments conducted to validate the individual functions of the sensors, with or without the flying robot, depending on the experiment. The final subsection outlines the experimental setup for an autonomous flight over a bridge, employing the developed and validated point sensor.

2.1. Robotic platform

A novel omnidirectional aerial system designed for contact-based inspection (Fig. 1 (a)) was used to carry out the experiments indoors and outdoors with several sensors placed on an end effector [30–32]. The hexacopter used actively tilting double rotor groups to exert forces during contact. Double rotor groups allowed the reduction of the overall system size and, therefore, the length of the end effector while generating enough thrust with a smaller rotor diameter.

The robot operated on two onboard batteries, offering a maximum flight duration of around 6 min. An alternative power source was an external power tether on the ground connected to the flying robot by a thin and lightweight wire. An external camera motion tracking system was used for indoor laboratory flights (section 3.3). For outdoor flights, onboard state estimation provided an estimate of the actual pose. Positional updates were given to the flying robot by a Leica Total Station (TS 50) for a stable flight without any drift and a reliable GPS signal. The position of the flying robot was detected with the help of a reflector (prism) continuously tracked by the total station. The robotic system was controlled onboard state estimation and control algorithms implemented in a Robotic Operating System (ROS) framework. Most of the information (flying robot and NDT measurements) was collected by ROS data collection tools and time stamped with respect to the same reference time using different acquisition rates.

For the outdoor flight path planning (section 2.5.5), a preliminary laser scan of the bridge was conducted using the Leica Total Station TS50. The resulting array of points from this scan was then converted to a triangular mesh with face and vertex normals using Poisson surface reconstruction, which could then be used for navigation and interaction planning. Force measurements were recorded with a Rokubi force sensor installed on the end effector. The desired polynomial trajectory was defined based on a grid of contact points projected onto the surface to be inspected. The spacing of the contact points was determined according to the inspection requirements. The orientation was defined by aligning the end effector axis to the surface normal obtained from the mesh reconstruction of the scanned surface. The gravity vector further constrained the hover orientation. A retreat distance from the surface parametrized navigation between points, and maximum velocities and accelerations were set to generate a smooth trajectory.

2.2. NDT-sensor at the end effector

The possibility to mount the end effector in different orientations relative to the flying platform allows for accounting for different surface orientations while maintaining an energy-efficient flight mode. The left side of Fig. 1 (a) depicts the robot with the horizontally oriented end effector with the mounted point sensor (details in section 2.2.1) in an orientation ideal for inspecting vertical surfaces. The right side of Fig. 1 (a) presents the flying robot with a wheel for overhead surfaces. The end effector orientation relative to the platform was tailored for inspecting overhead or inclined surfaces, such as the wheel sensor for HCP measurement and electrical resistance measurements of the concrete (details in section 2.2.2).

2.2.1. Point sensor

The point sensor is a customized RE mounted on a rigid end effector designed to conduct HCP measurements and electrical resistance mea-
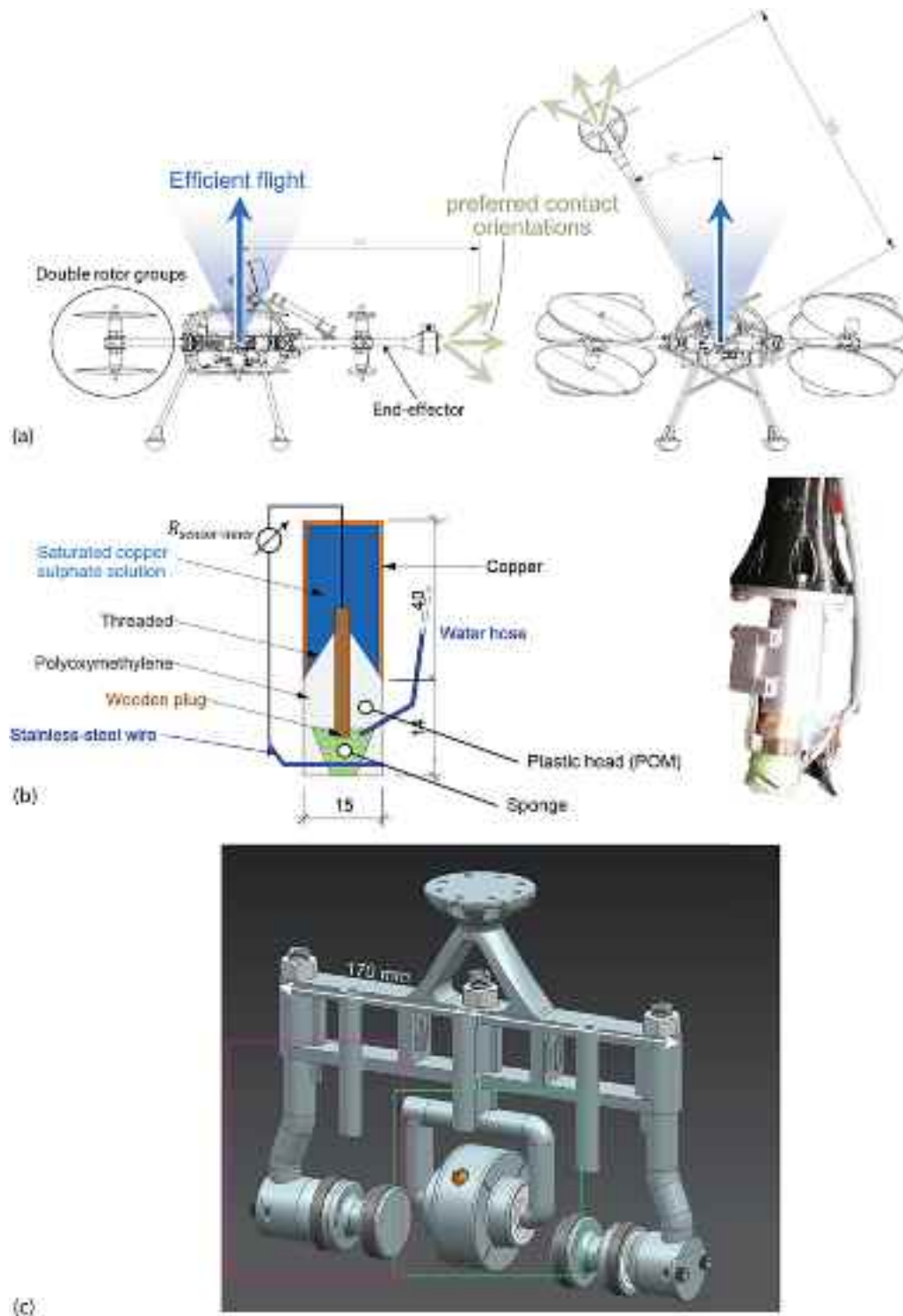
Fig. 1. (a) Efficient flight modes for the flying robot equipped with the point sensor or a wheel depends on the surface inclination of the target and the sensor orientation relative to the flying platform, (b) Sketch and image of the point sensor with the stainless-steel wire through the sponge at the tip of it for measuring the inner resistance of the sensor and the hose for tap water supply, as well as the produced sensor with the stainless-steel wire and the hose from the bottom mounted on the flying corrosion inspection robot and the 3D-printed part for the connection to the end effector, (c) illustration of the design of the combined rolling sensor for HCP measurements (potential measurement wheel in the violet box) and electrical resistance measurements in a four-point setup with a total width of 170 mm (resistance measurement wheels in the green box), and (d) detailed illustration of the potential measurement from (c) wheel once fully assembled and once in an exploded view with the four wooden plugs as diaphragms, the copper part in the center of the wheel, the two plastic bearings, the O-rings for the sealing system and the spring for damping and (e) detailed illustration from one of two resistance measurement wheels from the combined rolling sensor from (c) in an assembled and an exploded view with the main components consisting of stainless steel ring, bearing, slip ring, and the 3D-printed parts. (For interpretation of the references to colour in this figure legend, the reader is referred to the web version of this article.)
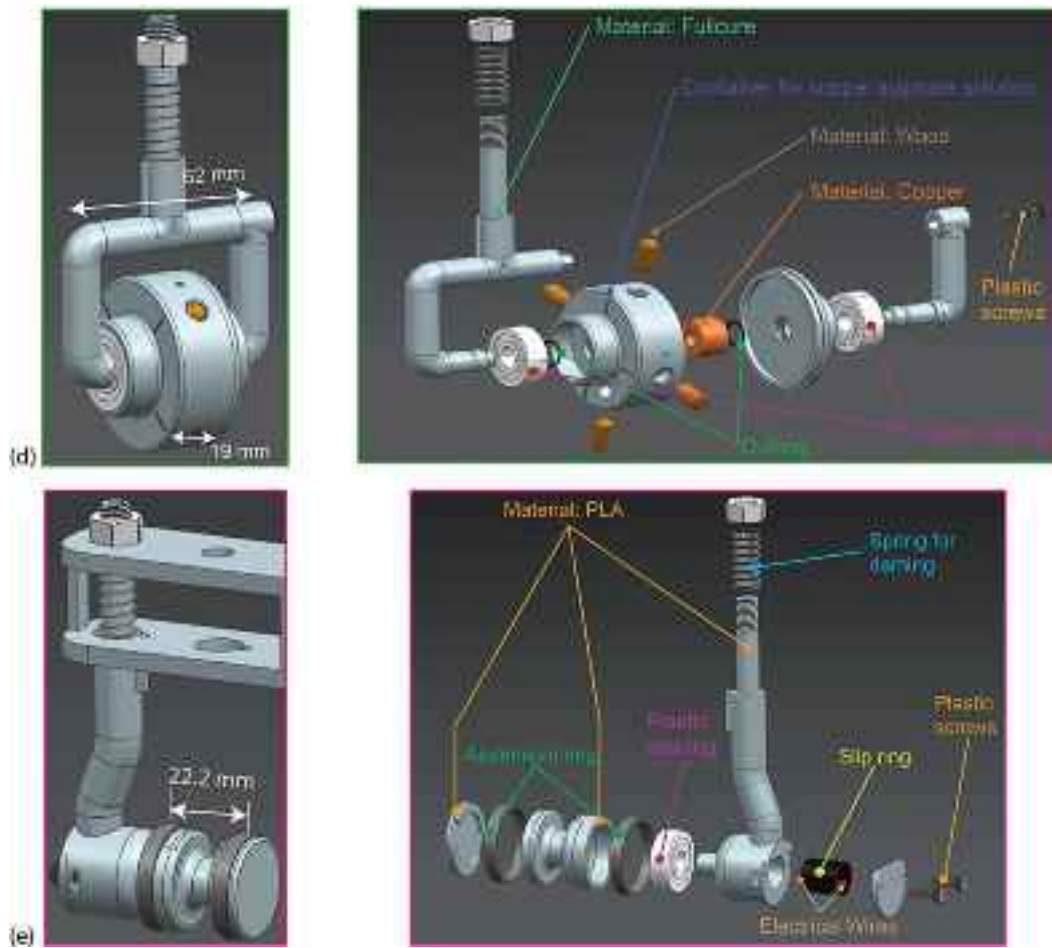
Fig. 1. (*continued*).

surements in a two-point setup. This setup allowed reliable measurement during autonomous inspection flights and fulfilled the requirements of the flying robot consisting mainly of weight and geometry constraints. The RE of the type copper/copper sulfate electrode (CSE) consisted of a copper tube and a plastic head. The plastic head is fixed on the threaded copper pipe with a threaded connection, as shown in Fig. 1 (b). A wooden plug, acting as the diaphragm, ensures the electrolytic connection between the solution and the wet sponge at the tip of the sensor head. The actual prototype of the RE weighted 30 g, fully assembled and in a functional state, including the copper sulfate solution [33]. At the tip of the point sensor, a stainless steel wire (diameter 1 mm) was passed through the sponge. The wire allowed for determining the inner resistance of the electrode ($R_{sensor-inner}$), which depends on the level of solution, the moisture state of the sponge, the orientation of the sensor, and the applied contact force. Contact forces cause deformation (squeezing) of the sponge up to the tip of the plastic head of the sensor, resulting in a change of $R_{sensor-inner}$. This $R_{sensor-inner}$, defined as the resistance between the copper part and the stainless steel wire (Fig. 1 (b)), allows correcting the electrical resistance between the sensor and the reinforcement obtained in a so-called 2-point setup [34] (section 2.4). The sponge was saturated with tap water using a peristaltic pump connected to a water hose (inner diameter 1 mm) to control the moisture state of the sponge, especially after repeated contact with dry concrete surfaces. The water hose ended at the electrode tip in an additional hole in the plastic head with a diameter of 2 mm.

2.2.2. Combined rolling sensor for the inspection of RC structures

Sensors in the form of wheels were introduced to improve the data collection efficiency with respect to the point sensor. Such a wheel

electrode was developed inspired by existing potential measurement wheels [23]. In addition to HCP, also the resistivity of the concrete could be measured by using the Wenner setup [35–37], respectively, with the more general Schlumberger equation [38] for unequally spaced electrodes. The prototype consisted of the potential measurement wheel in the center and four wheels (two on each side) to measure the electrical resistance of the concrete (resistance measurement wheels) (Fig. 1 (c)). The main requirement for the prototypes was to be as lightweight as possible so that the flying platform could control the sensor at the end effector. Further details of the materials used and a functional descriptions of the individual parts follow in the next sections.

2.2.3. Potential measurement wheel

The key objectives were to create a lightweight wheel electrode that maintains physical contact with the sensor while minimizing the non-contact phases, particularly during movement along possibly rough surfaces of RC structures. Additionally, the HCP mapping requires a constant electrolytic connection to the surface, which must always be maintained.

Early prototypes of the potential measurement wheel were used to check the functionality of the sensor. The focus was preventing leakages of copper sulfate solution during rolling, the repeatability of the measurement on a reinforced mortar block, and the detection of contact and non-contact phases with the electrochemical measurement. Electrolytic contact was ensured with a textile wrapped around the wheel that was kept moist with tap water prior to each measurement on the mortar specimen.

Figure 1 (d) shows the final design of the potential measurement wheel, including the dimensions and materials. The four wooden dowels

with a diameter of 6 mm ensured the electrolytic contact between the copper sulfate solution and the copper part inside and the concrete surface over an additional textile wrapped around the wheel. The thicknesses of the wheel wall (manufactured with 3D printer Objet3D Envy 350 V with FullCure as printing material) were between 2.5 mm and 4 mm. Two additional holes for maintenance were made on the wheel to fill or drain the copper sulfate inside the potential measurement wheel. Only one of the two maintenance holes is visible in Fig. 1 (d); the other was placed on the opposite side of the wheel to avoid a vacuum effect. The maintenance holes were closed with plastic M2 screws and with an O-ring. Two wires were connected to the copper part for redundancy. The shaft and the copper part were the stator in this application, while the wheel with the wooden dowels was the rotor. Two plastic bearings connected the stator and the rotor, enabling smooth rotation and preventing leakage of the copper sulfate solution. The conjunction between stator and rotor was an optimization problem with a conflict of objectives: on one end, the leakage prevention, and on the other end, the reduction of the rolling resistance. In fact, by reducing the friction of the rotary joint, the gap between the stator and rotor would increase, leading to a higher leaking rate. After optimization, the final sensor version had a total weight of 81 g in the fully functional state, including 17 g of copper sulfate solution.

Additionally, the 3D-printed prototype had certain limits regarding the precision of the printed part (0.1–0.03 mm) needed consideration. Small cavities near the O-ring, especially near the shaft and the outside of the container for the solution, were treated with grease. Hence, the sealing system was a combination of grease and two O-rings.

2.2.4. Resistance measurement wheels

Figure 1 (e) illustrates the design of the resistance measurement wheels for the flying corrosion inspection robot, highlighting the used materials and dimensions. The main parts were the aluminum rings, a plastic bearing, the slip ring, and the main body made of 3D-printed material Polylactic acid (PLA). The slip ring, also known as an electrical rotary joint, transmits electrical signals from a stationary to a rotary joint or vice versa. The slip ring had a diameter of 12.4 mm, a length of 14 mm, could connect to six wires, and weighed 4.65 g. The wires from the slip ring were fixed with pressure to the aluminum ring with a width of 2 mm, and any other movement was limited by filling the remaining space with epoxy. Per ring, two separate electrical connections were made at opposite sides of the aluminum ring for redundancy. The spring at the upper end of the sensor allowed a certain degree of compliance for the individual wheel to remain in contact with the concrete surface during the electrical resistance measurement. The main body of the 3D-printed part was built with a Prusa i3 MK3s printer with a reduced infill to optimize the weight of the overall sensor.

Experimental validation of this sensor component was conducted using aqueous solutions and concrete test specimens, as detailed in section 2.3.3. Furthermore, the electrolytic contact with the surface of specimens was ensured by wrapping a textile around the wheel and keeping it moist with tap water before each measurement.

2.3. Concrete specimens for validating the robotic platform and the sensors

2.3.1. Reinforced mortar beam for HCP measurements

Various experiments utilized two mortar beams with identical sizes and compositions of the mortar mix. The two specimens differed in the location of the chloride-containing mortar around the reinforcing steel; this mortar mix was intended to cause corrosion (anode) at a known location. The corroding spot was created by covering a part of 75 mm in length around the steel bar with chloride-containing mortar (3.75% chlorides by mass of cement) and was cast in 2013 [39]. The center of the chloride-containing mortar was at coordinates 10 and 20 cm in the two specimens, respectively. A schematic drawing of the specimens, including dimensions, is shown in Fig. 2 (a). The mortar had a water-to-binder ratio (w/b) of 0.6. The reinforcement bar had a diameter of 6 mm (B500B) and was positioned eccentrically to lead to concrete covers of
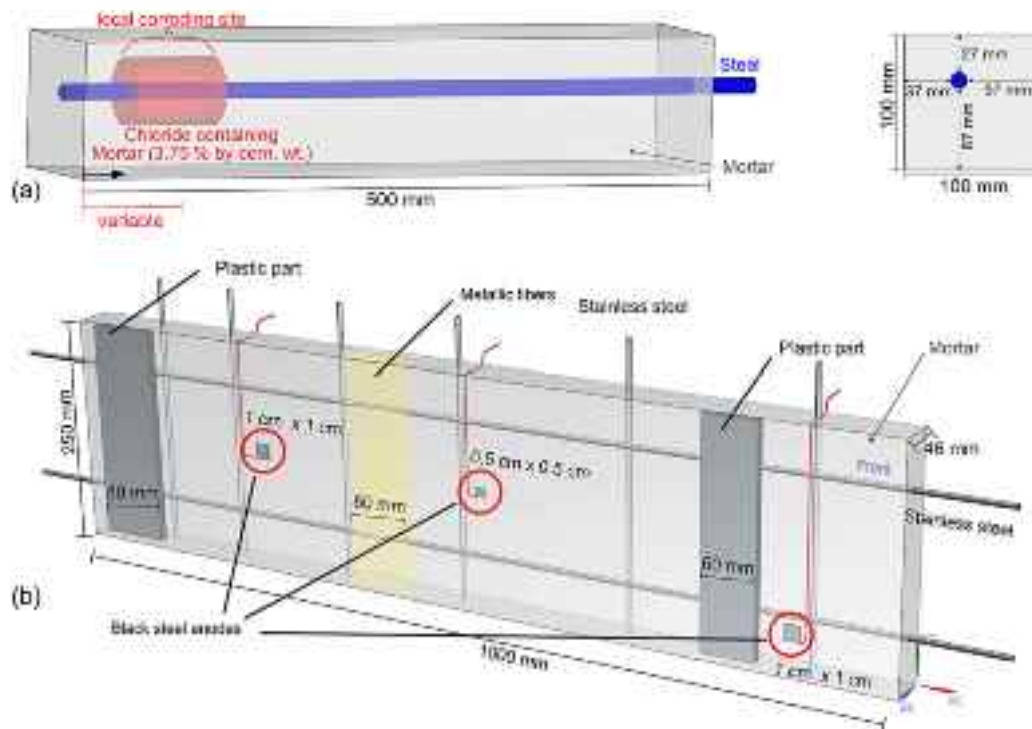
Fig. 2. (a) Schematic drawing of the reinforced mortar beam with an eccentrically placed reinforcement(B500B) and a part with chloride-containing mortar to create a local corroding spot (anode) by using 3.75% chloride by the weight of cement (by cem. wt.) and the indication of the water-to-binder ratio (w/b) of 0.6 and (b) Schematic drawing of the mortar block reinforced (w/b = 0.4) with a total of eight stainless-steel bars (∅ 6 mm) with three anodes of different sizes and two plastic parts for testing the combined wheeled sensor with the flying robot.

67, 57, 37, and 27 mm. The specimen was partially immersed in tap water along the longitudinal axis of the specimen on the side with the chloride-containing mortar.

2.3.2. Mortar cuboids for resistivity measurements

Three specimens were used to check the functionality of the resistance measurement wheels. The molds for the specimens were cubes with an edge length of 150 mm that were filled with the mortar mix, according to Table 1. The molds were filled up to heights of 56, 57, and 96 mm. The specimen with a height of 56 mm was stored in an indoor climate. In contrast, the other two specimens were stored in a controlled environment with 95% relative humidity (RH) and 20 °C prior to the experiments.

2.3.3. Mortar block for flight tests with the combined wheel sensor

The resistance measurement wheels were tested on a reinforced mortar block. The dimensions of the block are according to Fig. 2 (b) and the mortar mix from Table 1. The block was reinforced with eight stainless steel bars (∅6 mm): two longitudinally and six transversely. The block had three black steel anodes, two with a size of 1 cm × 1 cm and one with a size of 0.5 cm × 0.5 cm. All these anodes were electrically isolated from the stainless-steel reinforcement. Two anodes were located on the middle axis of the specimen, and one anode was placed eccentrically relative to the longitudinal axis. A 60 mm long section of the block contained hand-sprinkled steel fibers, introduced during casting to locally increase concrete resistivity. To locally increase the resistivity measurement, two plastic parts with lengths of 60 mm and 80 mm were included in the mortar block. The specimen was cured in a climate chamber for three days at 20 °C at 95% RH before removing the formwork.

2.4. Data analysis

This part describes the data analysis of the resistance data of the point sensor and the resistance measurement wheel and their conversion to resistivity. The electrical resistance and the resistivity are linked over a geometric factor (cell constant) that can be derived experimentally or with numerical simulations [35,40–43]. This section describes the determination of the cell constant for the point sensor (2-point setup (2p)) and the resistance measurement wheels (4-point setup (4p)).

The point sensor measured the electrical resistance in a so-called 2-point (2p) setup [11] between the sensor (internal copper rod) and the reinforcement. According to the literature [34, 35], the measured resistance R can be converted to resistivity ρ by:

$$\rho = 2 \cdot d \cdot R \tag{1}$$

Here, d is the diameter of the probe. The method is only recommended if the cover depth is thicker than twice the diameter of the probe [34]. This equation converted the resistance measured with the point between the sensor and the reinforcement sensor ($R_{2p-Sensor}$) to a resistivity ($\rho_{2p-Sensor}$) value.

The so-called Wenner setup is often used for resistivity measurements [37]. The Wenner configuration with four equally spaced electrodes is a particular case of the Schlumberger setup, where not all electrodes are equally spaced. The Schlumberger equation (eq. (2)) is written by:

$$\rho = \pi \cdot R \cdot \frac{c \cdot (c + d)}{d} \tag{2}$$

The parameter d is the spacing between the inner two electrodes, and the parameter c is the spacing between an outer wheel to the geometrically closer inner wheel. This equation will be used to convert the resistance obtained by the resistance measurement wheels ($R_{4p-wheels}$) to resistivity ($\rho_{4p-wheels}$) value.

The Wenner equation is, in theory, valid for homogenous semi-infinite spaces with homogenous resistivity [11,35]. However, the analysis of Angst and Elsener showed that the Wenner equation is still applicable to measure the apparent resistivity of concrete, even if some theoretical assumptions are violated [35]. Due to geometrical limitations caused by the potential measurement wheel in between the two inner wheels of the resistance measurement wheel, it was not possible to use the Wenner setup. However, it is assumed that the error in the resistivity is in the same order of magnitude as for the Wenner setup.

2.5. Experiments

This part of the paper presents the different assessments of the point and the wheeled sensors in the laboratory with a camera motion tracking system and outdoor flights with external state estimation. The outdoor experiment was conducted on a box girder bridge in Switzerland, serving as a real-world validation following successful trials in controlled settings. The onboard state estimation, in combination with absolute position measurements from a Leica Total Station, eliminated the need for an external camera motion tracking system used during indoor flights. Table 2 presents an overview of the eight different experiments and their goals.

2.5.1. Assessment of the wetting procedure for the point sensor

There must be sufficient electrolytic contact between the RE and the concrete surface to obtain a reliable potential measurement. If not, the concrete surface should be pre-wetted as recommended in guidelines about HCP mapping [10,12]. Furthermore, the sensor might sustain damage during uncontrolled contact with the concrete surface established by the control of the flying robot. Therefore, for automated measurements during an autonomous flight, a suitable procedure was required to check the sensor's functionality and ensure sufficient

Table 1
Mortar mix for cuboids and the mortar block.

Material	Weight proportions [−]
Ordinary Portland cement (CEM I)	1
Water	0.4
Aggregate0/4	2.5
Superplasticizer (Glenium ACE 30)	0.01
Admixed chlorides	0.012

Table 2
Overview of the experiments conducted on the individual parts of the sensors attached at the end effector of the flying platform.

Testing	The goal of tests carried out	Results presentation in section
Point sensor	Inner resistance as a measure of moisture in the sponge to monitor the functionality of the probe	3.1
Potential measurement wheel	Check repeatability, leakage of the solution, reliability of the signal	3.2.1
Resistance measurement wheels	Determine the cell constant of the Schlumberger method in solution and verify measurement on a mortar block compared to uniaxial tests.	3.2.2 3.2.3
Point sensor	Comparison of results (HCP and electrical resistances) obtained with the flying robot to a human operator	3.3.1
Potential measurement wheel	Comparison of results (HCP) obtained with the flying robot to a human operator	3.3.2
Resistance measurement wheels	Perform autonomous measurements with the resistance measurement wheels on a mortar beam while rolling horizontally or vertically	3.3.3
Point sensor	Final test of the flying inspection robot on a bridge	3.3.4

electrolytic contact.

The experimental setup included a robotic arm (Mitsubishi RV-2AJ), a reinforced mortar beam (section 2.3.1), and the point sensor (section 2.2.1). The mortar beam was stored in an indoor room climate (20 °C, ~50 R.H.) for several weeks before the experiment was conducted to achieve a low moisture content in the cover concrete. The sponge was wetted with tap water before the experiment and completely saturated. The point sensor (see section 2.2.1) was fixed with clamps at the robot's end effector with vertical orientation, with the tip of the sensor pointing towards the ground. The robotic arm moved the probe sequentially to predefined coordinates on the mortar beam with a spacing of 10 mm × 10 mm to avoid overlapping the already contacted areas, taking into account margins of 30 mm on the sides of the beam. With these restrictions, the surface of the block could accommodate 176 contact points, arranged in 4 rows and 44 columns. The predefined coordinates constrained all movements of the robotic arm; no force control was available, and the robot arm placed the sensor perpendicularly on the surface. In between the measurements on the beam, the resistance between the stainless-steel plate and the copper part of the probe was determined on a stainless steel plate for a control measurement of $R_{sensor-inner}$. This assessment presumed the steel's electrical resistance was negligible, implying that the measured resistance reflected the (moisture) condition in the sponge. An overview of the contact points on the specimen and the procedure for evaluating the wetting process of the point electrode is given in Fig. 3.

A BK-Precision 879B LCR-meter measured the AC resistance with a frequency of 120 Hz and V_{rms} of 0.75 V on the stainless-steel plate. The final result, derived from the average of three readings, was obtained within an approximate 3 s contact duration. On average, measuring a single point—comprising beam contact and electrical resistance assessment—took between 10 and 15 s. The time span for measuring a single point was not constant due to the fixed velocity of the movements controlled by the robotic arm.

2.5.2. Assessment of the potential measurement wheel

The potential measurement wheel was tested in two setups focused on detecting leaking solution, non-contact phases with the concrete surface, and repeatability. The specimen was a mortar beam, as described in section 2.3.1. Before the experiment, the specimen was conditioned in a controlled environment at 20 °C and 95% RH for several days.

During the first experiment, the wheel electrode was moved by hand six times over the specimens on the side with a concrete cover of 27 mm. The objective was to test the repeatability of the measurement taken with the potential measurement wheels. The second experiment aimed to detect phases with and without contact with the concrete surface through electrochemical measurements. The length of the concrete specimen was split into nine equally long segments with a length of 5 cm. The potential measurement wheel was moved by hand until the end of each segment and then lifted for approximately 1 to 2 s, and the subsequent segment was measured. This procedure was repeated until the end of the specimen. The HCP data were recorded in both experiments with an Autolab PGSTAT 30 of Methrom AG with a sampling frequency of 20 Hz. After the experiment was completed, the potential measurement wheel was checked for leakage of copper sulfate solution.

2.5.3. Comparison to manually taken measurements

Data acquired by the flying robot, using either the point sensor or the potential measurement wheel, were benchmarked against manual measurements in a similar experimental setup. The functionality of the point sensor was checked on a mortar beam (section 2.3.1.) on the side with a cover of 27 mm. In this experiment, the ability of the flying robot to maintain the necessary positional precision and the ability to apply sufficient force for conducting reliable HCP measurements on structures was tested. Finally, the measurements were compared to measurements taken by a human. The flights were carried out in the laboratory with a camera motion tracking system. The rigid end effector was equipped with the point sensor that measured HCP values and electrical resistances between the sensor and either the reinforcement or the stainless steel wire at the tip of the sensor. External state estimation determined the concrete block's position. Based on these coordinates, trajectories were created to contact nine locations spaced at 5 cm intervals along the surface autonomously. Each position was maintained for 10 s while a reference force of 5 N was estimated to ensure sufficient contact. The operator visually determined the contact of the sensor on the block and then started the measurement procedure. The procedure consisted of 35 readings with a Keithley multimeter model 2001 and electrical resistance measurements ($R_{sensor-inner}$ and $R_{2p-Sensor}$). Each electrical resistance data point was the mean value of three measurements, which were taken with a BK-Precision 879B LCR-meter (120 Hz and V_{RMS} of 0.75 V).

The functionality of the potential measurement wheel was tested on a mortar beam on the side with a cover of 57 mm. Measurements were taken with the flying robot while the block was horizontally or vertically oriented. The vertical flights were performed while rolling the wheel from top to bottom. The local planner generated the trajectory by setting waypoints along the mortar block. This experiment aimed to show the versatility of taking measurements with the potential measurement wheel mounted on the flying robot and confirm similar results compared to measurements taken by hand.
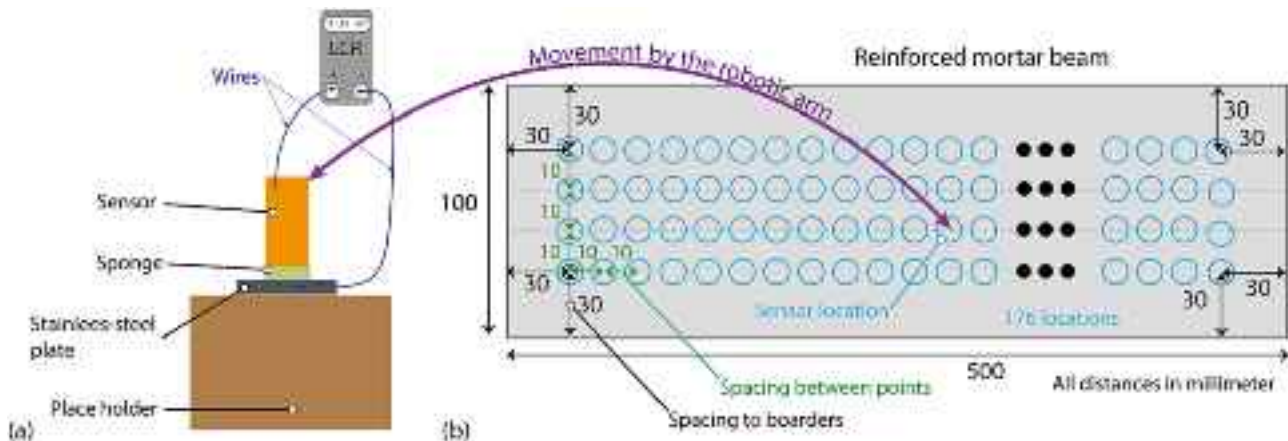

Fig. 3. (a) Assessment of the inner resistance of the point sensor ($R_{sensor-inner}$) on a stainless steel plate by means of the use of a robotic arm and an LCR meter and (b) top view of the reinforced mortar beam with the 176 measuring points on the surface. The three black dots per horizontal measurement line represents the missing sensor locations in the sketch along the block.

2.5.4. Experimental validation of the resistance measurement wheel on a mortar beam

This subsection is divided into three parts. The first part involves the experimental determination of the cell constant of the sensor in solutions. This is followed by a comparison of the measured resistances from mortar specimens after the conversion to resistivity against resistivities derived using the uniaxial method. The last step was the final test of the resistance measurement wheels on a mortar block, where the resistance was measured at discrete locations or while rolling with the sensor over the beam.

The cell constant of the resistance measurement wheels was determined using nine different solutions made of distilled water with different concentrations of sodium chloride. The conductivity, measured with a SevenExcellence conductivity meter, varied between 17.5 µS/cm and 17,100 µS/cm. The resistivity of these solutions ranged from 0.6 Ωm up to 570 Ωm, the latter comparable to concretes with ordinary Portland cement for an outdoor climate exposed to the weather [11]. The resistivity is the product of the cell constant and the resistance. A linear regression with the least squares method was used to determine the cell constant of the sensor based on resistance measurements with the resistance measurement wheels and the resistivity of the solutions. The cell constant was determined in a plastic container measuring 365 mm × 565 mm × 200 mm, filled to a height of 100 mm with the different solutions, all at an ambient temperature of around 22 °C. The resistances were measured with Methrom Autolab electrochemical workstation with 31 distinct AC frequencies between 10 Hz and 10 kHz with an amplitude of 0.3535 V_{RMS}. Alternatively, the cell constant could also be calculated with the Schlumberger equation (eq. (2)). To determine the cell constant, the distances between the four electrodes of the resistance measurement wheels must be known. The distance between the two wheels on the same axis was 22.2 mm (Fig. 1 (e)). The distance between the inner two wheels (left and right of the potential measurement wheel was 81.6 mm (Fig. 1 (c).

The experimentally determined cell constant was checked against uniaxial resistance measurements on mortar specimens (section 2.3.2). The resistance of the specimens was determined using an Autolab with 31 AC frequencies between 10 Hz and 10 kHz with an amplitude of 0.3535 V_{RMS}, similar to the procedure used to calculate the cell constant. Both sides of the mortar specimens were covered with moist textiles (tap water) for the uniaxial test with a known geometrical factor because of the geometry of the specimens [11]. This experiment was performed in all three possible orientations (top to bottom, opposite faces on the lateral sides) to estimate the homogeneity of the specimen. All wheels of the sensor were covered with textiles and moistened with tap water prior to the experiment. The sensor was positioned diagonally on the block to optimize the distance from the cube edges, thereby minimizing measurement errors [35]. The resistances of these three specimens were measured with the same procedure with a Autolab as before and averaged. The experimentally obtained cell constant transformed this averaged resistance ($R_{4p-wheels}$) into a resistivity value ($\rho_{4p-wheels}$).

The beam (section 2.3.3) was tested with the resistance measurement wheel while measuring the resistance every 5 cm along the surface while the wheel was not rolling. A GAMRY 1010E or a Methrom Autolab were used as electrochemical workstation to measure the impedance for 31 frequencies between 10 Hz and 10 kHz. The $R_{4p-wheels}$ was transformed into $\rho_{4p-wheels}$ using the experimentally determined cell constant with the procedure described above. The final test was performed with the flying robot while moving the resistance measurement wheels slowly over the mortar surface to acquire reliable resistance measurements. The sampling frequency of the GAMRY was constrained to around six measurements per second (slightly dependent on the frequency), which ultimately limits the maximum driving speed of the flying robot. Compared to initial experiments with speeds exceeding 1.0 cm/s, the driving speed was adjusted to a range of approximately 0.4 cm/s to 0.5 cm/s to ensure reliable results. This driving speed was utilized to compute the position vector along the specimen, assuming the same beginning and ending points on the block and a constant velocity.

2.5.5. Outdoor flight with the flying corrosion inspection robot

An outdoor flight was performed on a pre-stressed box girder bridge in Switzerland (Fig. 4 (a)). The inspection task for the robot was to fly autonomously towards the longitudinal girder near one back wall of the bridge to collect data with the point sensor mounted on the end effector and placing the sensor perpendicular to the surface. The objective was to autonomously collect a potential map and concrete electrical resistances, and to do so, outside of laboratory conditions, exposed to external factors such as wind and changing light, all while utilizing onboard state estimation. Fig. 4 (b) shows the flying corrosion inspection robot in the air equipped with the point sensor approaching the bridge and the total station.

Figure 5 gives an overview of the interaction of the different components of the flying corrosion inspection robot and how they interact. While the robot did not actively control the peristaltic pump, the operator had the capability to adjust its rotation speed, thereby controlling the water flow during an experiment. The potential measurement was performed with a benchtop multimeter from Keithley (model 2000). The device, connected to the base station with a General Purpose Input/Output (GPIO) to a USB connector, measured the potential difference between the reinforcement of the bridge and the sensor. Onboard batteries supplied the power for the flying robot.

After determining the desired ten contact points in a grid of 20 cm × 20 cm and calculating the trajectories for the flying robot to reach these coordinates with the end effector. The flying robot's take-off position was approximately 2 m horizontally and 1.5 m vertically below the first measurement point (see Fig. 4 (b)). Before the take-off (see Fig. 14), the sponge was fully saturated with tap water that was continuously provided by a peristaltic pump (Fig. 5). After the take-off, the flying robot autonomously contacted the first point with the point sensor. The operator visually ensured that a stable contact was achieved, then started the NDT measurement capture process started. The measurement protocol included 40 potentials with a measurement frequency of 10 Hz followed by five measurements of $R_{2p-Sensor}$ with a measurement frequency of 0.7 Hz with the LCR-meter (BK-Precision 879B, 120 Hz and V_{RMS} of 0.75 V). After NDT-data acquisition was completed, the operator sent the signal to approach the next point to repeat the procedure. Owing to safety considerations related to the robot's limited battery flight time, only 10 points on the structure were targeted.

3. Results and discussion

3.1. Point sensor assessment

Figure 6 shows the evolution of $R_{sensor-inner}$ after an initial saturation of the sponge with tap water, followed by 176 contact points on a dry mortar surface determined with the procedure described in section 2.5.1. The $R_{sensor-inner}$ showed an almost negligible increase for the first approximately 100 measurements despite a few points with higher internal resistance. This part was followed by a steep increase in the inner resistance with the number of points measured.

Evaluation of the point sensor indicated a need to re-saturate the sponge at the electrode's tip after a specific count of measurements. In this experiment, around 100 measurements yielded a negligible increase in $R_{sensor-inner}$ values. However, this number depends on several factors, such as concrete surface moisture or contact pressure. Consequently, this number of touches of the point sensor and the concrete surface with a negligible $R_{sensor-inner}$ should be considered as a recommendation, and continuous monitoring of $R_{sensor-inner}$ is advised. The water hose into the probe (Fig. 1 (b)) allows for wetting the sponge with tap water during a flight with the robot. The continuous wetting of the sponge will contribute to reliable measurements of the electrical resistance and the HCP values during an autonomous flight with the robot.

Fig. 4. (a) Image of the box girder bridge, on the location where the autonomous inspection flight took place and (b) flying corrosion inspection robot equipped with the point sensor. A safety tether connected to the robot from above adds security for experimental testing, and cables from below connect a water supply (peristaltic pump) and electrode signal to the platform.

3.2. Wheeled sensors

3.2.1. Assessment of the potential measurement wheel

Figure 7 presents the potential for six trials along the mortar beam (section 2.3.1). The potential measurement wheel was rolled by hand over the surface, maintaining contact as elaborated in section 2.5.2. The wheel electrode was pressed onto the concrete surface by hand with adequate pressure, ensuring it rolled smoothly without dragging.

All lines show the same pattern: a decrease in the potential of around 75 mV towards the coordinate 20 cm followed by a gradual increase of the potential to roughly 0 mV vs. CSE at the right end. The coordinates of the lowest potentials per trial correspond to the location of the chloride-containing mortar at a coordinate of 20 cm. The potentials closer to the coordinate 0 cm were notably lower than those at coordinates range between 35 and 50 cm. This difference can be explained by the partial immersion of the left end of the specimen (near the chloride-containing mortar). Submerging the specimen in water led to a higher local moisture content of the concrete. Higher moisture states generally decrease HCP values [44].

Time-to-distance conversion was conducted without relying on odometry data, assuming a uniform driving speed across the 50 cm beam. This necessary stretching or shrinking of the data in space explains that the lowest potential value was not precisely at a similar location for all six measurements.

The second experiment, conducted on the same beam, involving the lifting the wheel at 5 cm intervals to check the ability to detect non-contact phases with HCP measurements. Lifting the sensor off the

mortar specimen resulted in a distinctly different potential. During these non-contact phases, values of −10 V vs. CSE or + 10 V vs. CSE were recorded. These extremely high or low potentials compared to ranges for steel in concrete made it feasible to remove these potential values with a simple filter [42]. These filters rejected values above or below a certain threshold.

Figure 8 (a) shows the raw data of the three trials of the experiment in a potential range between −250 mV vs. CSE and 50 mV vs. CSE over time. Potential values near −10 or + 10 V vs. CSE for non-contacted phases were not displayed to compare the results better to the filtered and post-processed representation in Fig. 8 (b). A 10 vertical lifting-off of the potential measurement wheel for one to two seconds was already visible in the time-plotted data ahead of further post-processing, resulting in 10 distinguishable segments, marked by arrows in Fig. 8 (a). The data filtering approach removed potentials of values −10 V vs. CSE or + 10 V vs. CSE and gradients larger than $2500 \frac{mV}{s}$. The last filter was a Savitzky-Golay filter (window length of 3, second-order polynomial) to eliminate single potential values in the signal that remained from the lifting-off phases of the potential measurement wheel.

Fig. 8 (b) presents the ten segments after the conversion from time to distance, based on an assumed consistent driving speed across each 5 cm beam segment. This representation allows a better comparison of the potentials between the three trials and the results from Fig. 7. The most negative potentials were measured near the part of the steel covered with chloride-containing mortar and between 15 cm to 25 cm along the beam, similar to the results from the continuous rolling with the potential measurement wheel (Fig. 7).

Fig. 4. (*continued*).

The leftmost segment exhibited the largest differences between the three trials. After the third segment, the differences between the potential values of the three trials in the segments decreased. There was a potential difference between the last potential of each segment and the subsequent starting potential value of the next segment. Several possible sources contributed to this potential jump. Lifting and positioning the wheel at the correct location was crucial to obtain a continuous line for each trial. For example, lifting the wheel before or after the end of the segment could contribute to potential differences, as visible for trial 1 between segments 8 and 9. In addition to the limited positional
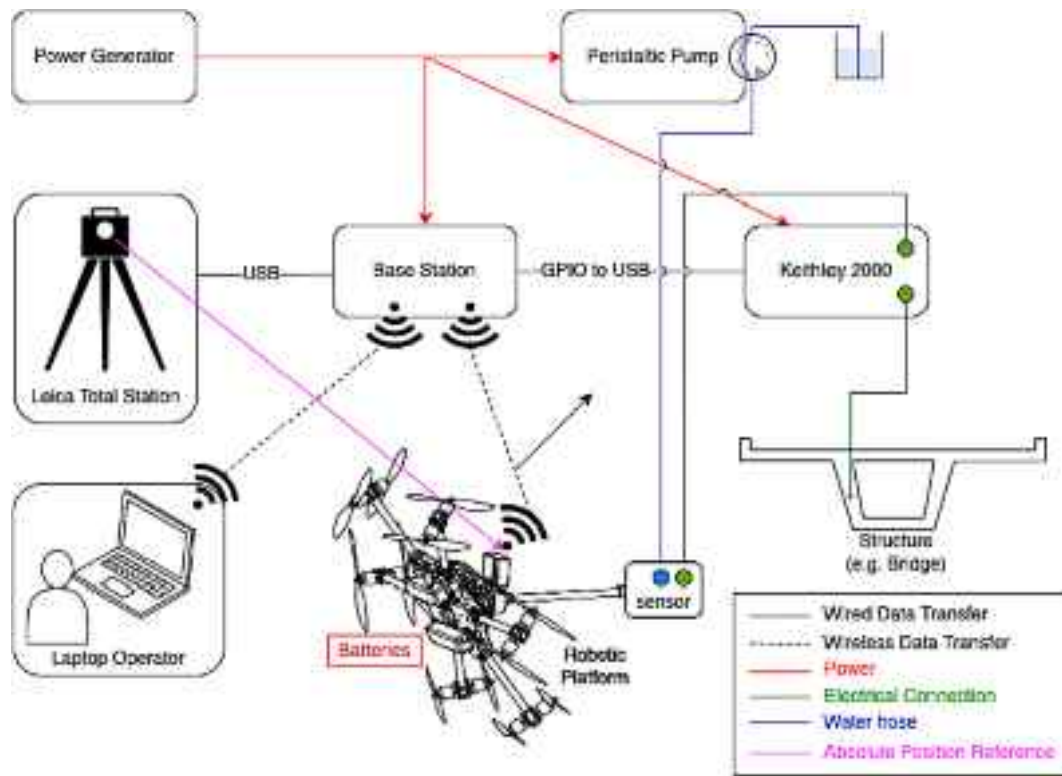
Fig. 5. Overview of the system with the flying robotic platform and the devices to enable the HCP mapping in the outdoor experiment in an autonomous way on the box girder bridge.
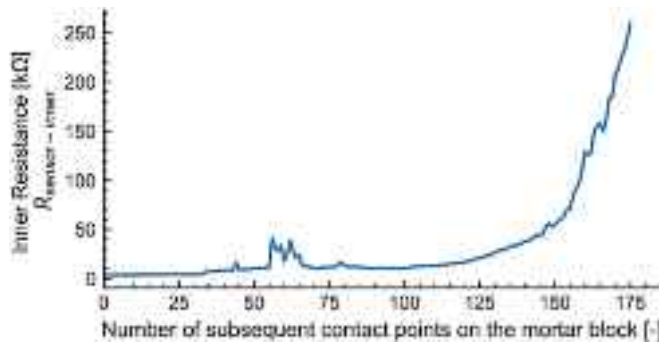

Fig. 6. Assessment of the inner resistance of the RE on a reinforced mortar beam with 176 different contact points with the dry surface and measurements of the inner resistance on a stainless-steel plate showing a steep increase of the inner resistance after approximately 100 measurements.

Fig. 7. Results obtained with the potential measurement wheel on the mortar beam for six consecutive measurements on the identical specimen while the wheel was moved by hand over the identical specimen. The lowest potentials for all trials were measured near the chloride-containing mortar at 20 cm.

accuracy, the data filter might have removed too many or too little data from the filters. Nonetheless, the primary objective was the automated detection of both contact and non-contact phases using an appropriate method. This detection can be refined by using force sensor data.

These two laboratory experiments showed that the design of the potential measurement wheel works reliably. The sealing system of the sensor retained the copper sulfate solution efficiently during the measurements and was therefore considered to be functional.

3.2.2. Resistance measurement wheel

The cell constant was determined to be 0.0724 m for the resistance measurement wheels. Within the applied frequency range, the impact on impedance was minimal. This experimental cell constant was slightly lower than the one obtained by the Schlumberger equation (eq. (2)) with a value of 0.08823 m.

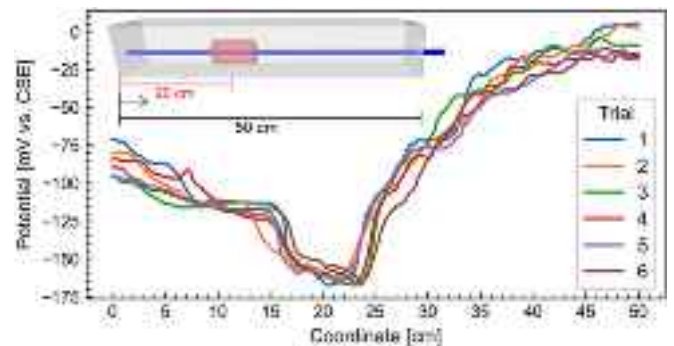Resistivity values obtained with the resistance measurement wheels

were compared to ones obtained by uniaxial resistance measurements on mortar specimens. Table 3 provides an overview of the results from both the resistance measurement wheel and uniaxial resistance measurements. The deviation between the two methods was between 2 and 18%. The mean of the uniaxial resistance measurements led to a difference of around 5% between the two specimens with different heights stored under the same condition. This experiment demonstrated the applicability of the solution-determined cell constant to mortar test specimens. It's noteworthy that all measurements were conducted without any wheel movement.

In general, the resistivity obtained by measurements with the resistance measurement wheel slightly overestimated the results by the uniaxial test. Differences were probably caused by the different areas of textile and mortar contact and the uptake of tap water from the textile into the pore structure of the mortar or by the geometrical limitations of

(a)

(b)
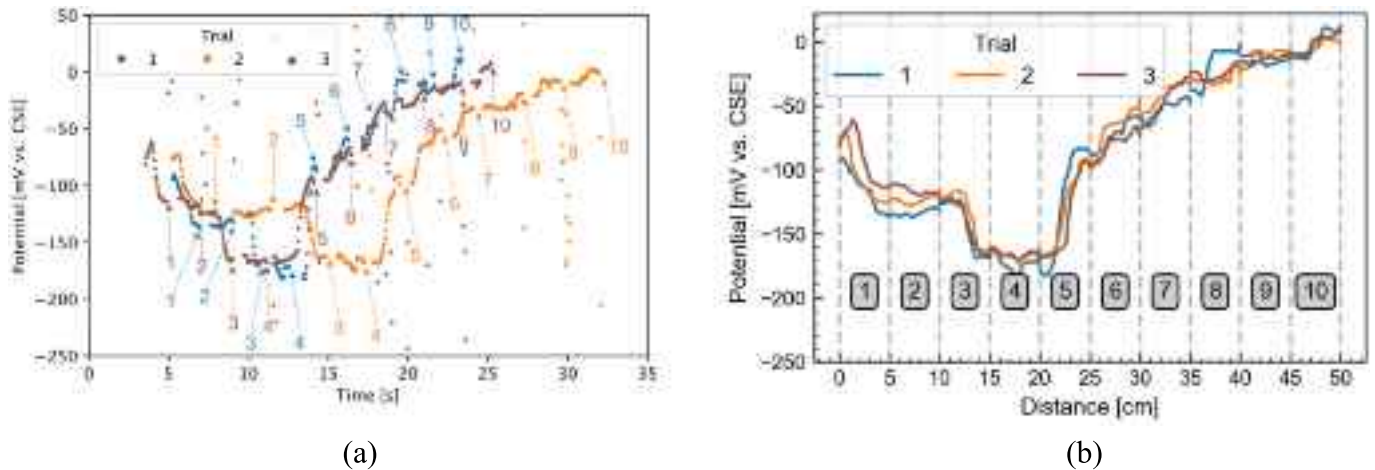
Fig. 8. Potential data from the three trials in the same experiment in which the potential measurement wheel was lifted vertically by hand every 5 cm for 1 to 2 s on a mortar beam. (a) Raw data in the potential range between −250 mV vs. CSE and 50 mV vs. CSE with the indication of the ten lifting-offs of the RE per trial and (b) filtered data and converted to distance while assuming a constant velocity in the ten segments (subsequently numbered in the grey boxes) with a length of 5 cm. The minimum potentials for all tests were recorded close to the mortar containing chloride at a distance of 20 cm.

Table 3

Overview of the mortar specimens to measure the resistivity wheels on three different specimens and compare the uniaxial resistance measurement at 5 kHz to these results with the experimentally derived cell constant.

	Specimen		
	Block I	Block II	Block III
Storage condition	Laboratory environment	20 °C, 95 RH	20 °C, 95 RH
Height [mm]	57	56	96
Mean of the uniaxial resistance measurements [Ωm]	124.4	71.5	66.8
Resistance measurement wheel [Ωm]	127.5	84.5	70.3
Difference [Ωm] (Change [%])	+3.1 (2.4)	+13.0 (18.2)	+3.5 (5.2)

the specimen [35].

3.2.3. Experiments on the concrete block with the resistance measurement wheel

Figure 9 shows the result of the manual assessment with the resistance measurement wheels on the mortar block with varying resistivity (see section 2.5.4) The two plastic pieces inside the block may be recognized at distances of 5 and 80 cm when a much higher resistivity was measured compared to other measurements on the block. The addition of metal fibers (around 40 cm away from the left end) in the mortar mixture did not affect the electrical resistance respectively, the resistivity.

The results obtained by the resistance measurement wheels allowed to clearly distinguish between surface areas with higher and lower resistance. These findings provide a basis for comparing experiments where the resistance measurement wheels, attached to the flying robot, roll over the identical surface.

### 3.3. Indoor and outdoor flights

3.3.1. Point sensor

Figure 10 (a) shows the autonomously recorded median potential value of two flights alongside manually measured potentials along the mortar beam. Manual measurements were conducted multiple times both before and after the two flights. Fig. 10 (b) compares the electrical resistance measurements between the sensor and the reinforcement and the electrical resistance between the sensor and the wire at the sponge of

the RE on the mortar beam. The electrical resistance measurements between the sensor tip and the reinforcement were converted to resistivity using eq. (1). All measurements, whether taken manually or with the sensor mounted on the end effector, were conducted on the side with a 27 mm concrete cover.
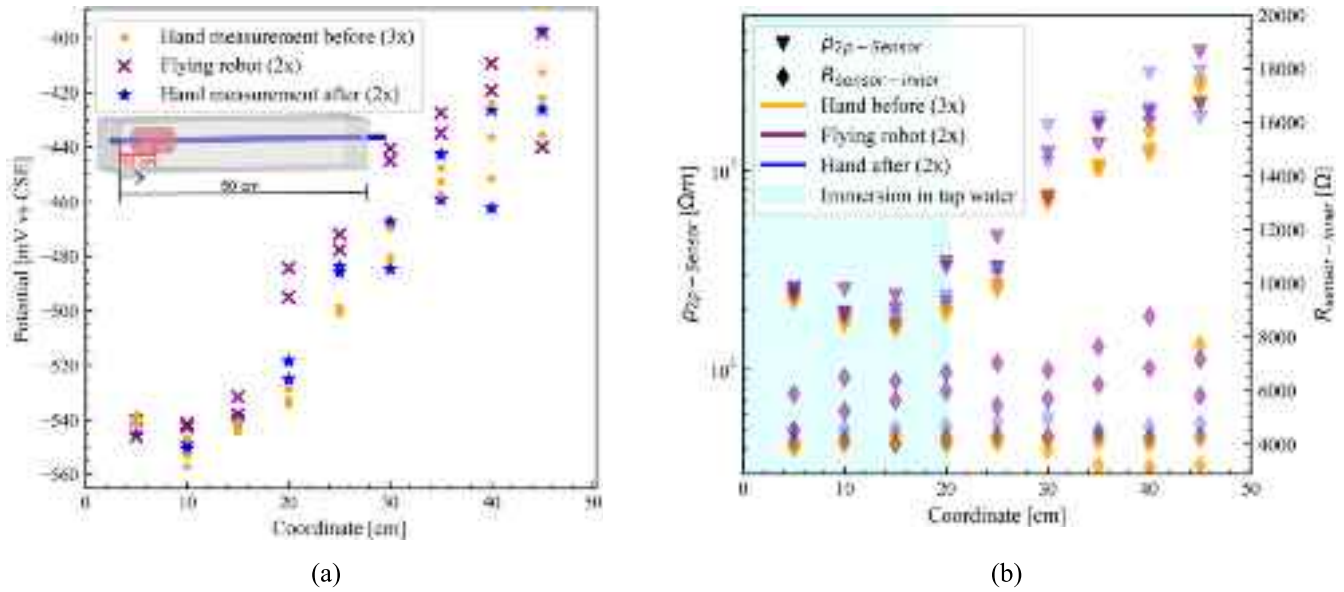
Measurements taken by hand and with the flying robot yielded similar results for the median of the HCP measurements. The lowest potentials per measurement coincide with the location of the chloride-containing mortar from the specimen preparation (section 2.3.1). The potential readings on a measurement point on the beam were nearly constant over time, except for the first few measurements at certain locations. This finding suggests that the flying robot could apply sufficient force over the end effector for reliable HCP measurements. Differences in the potential may arise due to the drying process of the specimen, and spatial deviations of the contact position, especially while using the flying robot. Nonetheless, this comparison confirmed that potential readings with the robot were comparable to measurements by human operators.

The values for the mean of the electrical resistance measurements ($R_{2p-Sensor}$), respectively $\rho_{2p-Sensor}$ obtained using the linear transformation using eq. (1), were comparable, irrespective of whether the measurements were carried out manually or with the flying robot. In general, the electrical resistance increased from left to right, respectively, from lower to higher coordinates along the x-axis for the
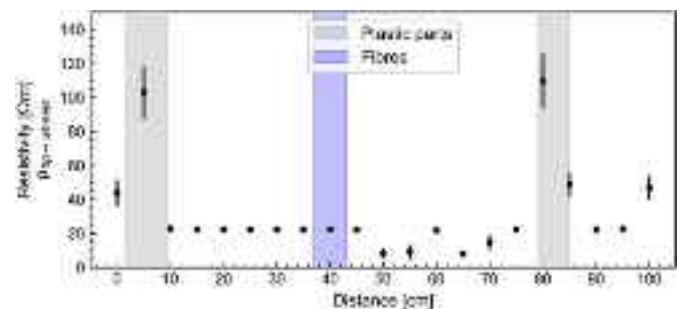
Fig. 9. Resistivity measurement on the mortar block with a length of 1000 mm (2.5.4). The electrical resistivity was calculated with the cell constant of 0.0724 m. The mean value is displayed with the standard deviation of the 31 frequencies between 10 Hz and 10 kHz, and the vertical line is the standard deviation of the measurements at each location. The resistance measurement wheels were manually moved in steps of 5 cm over the block by measuring with a GAMRY 1010E while the wheel was kept fixed at each location.

(a)   (b)

Fig. 10. (a) Comparison of the mean potentials between conventional measurements by hand before and after the measurement with the flying corrosion inspection robot equipped with the point sensor and (b) comparison of the resistivity between the sensor and the reinforcement bar ($\rho_{2p-Sensor}$) and the inner resistance of the sensor ($R_{sensor-inner}$) by placing the sensor by hand to the RC beam in comparison to measurements with the flying robot.

electrical resistance towards the end of the specimen. The increase in the resistivity was approximately one order of magnitude. The lowest resistivity between the sensor and the reinforcement were measured at the area (near coordinate 10 cm) where the chloride-containing mortar was located.

The $R_{sensor-inner}$ did not vary significantly due to the constant tap water supply during the experiments. The differences between measurements taken by hand and with the flying robot vary for various reasons. On the one hand, the sponge was saturated for each measurement taken by hand. As mentioned before, a higher moisture generally affects the electrical resistance. On the other hand, the flying robot rapidly dried the surface of the specimen with the turning rotors during hovering. This might have lowered the electrical resistance measurement at the following point. An increase in $R_{sensor-inner}$ was not expected due to the assessment results of the point sensor (section 3.1).

3.3.2. Potential measurement wheel

Figure 11 presents the nine measurements obtained with the flying
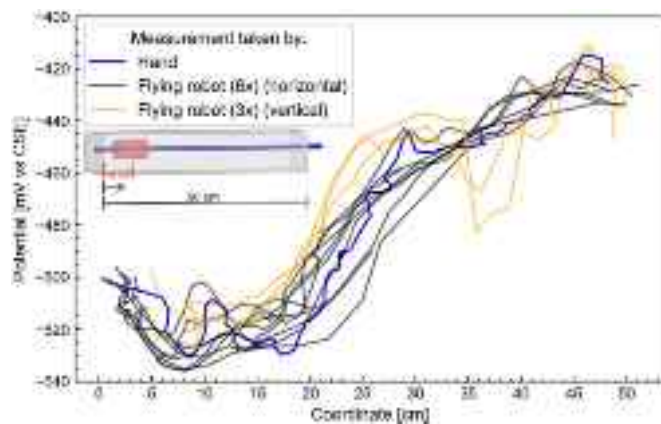
Fig. 11. Potential readings along the reinforced mortar beam for different trials while rolling with the potential measurement wheel horizontally or top to bottom along a mortar specimen (described in section 1.3.1) obtained with the flying robot compared to a measurement taken by hand while rolling on the identical specimen.

robot compared to the measurements taken by hand. The measurements were performed on the horizontally (left to right) or vertically (top to bottom) oriented mortar beam, as described in section 2.5.2.

All trials on the beam exhibited a consistent behavior: a potential decrease between the 10 and 20 cm coordinates, followed by an increase up to −420 mV vs. CSE near the right end of the specimen. The corrosion spot was positioned at the 10 cm coordinate for this specimen. The lowest potentials coincide with the area where an anode is expected based on specimen preparation. The similar potential curve along the specimen confirms the repeatability of the HCP mapping using the wheel electrode. Moreover, the results were similar to the measurements taken by hand.

Most of the time, the potential measurement wheel was rolling, but occasionally, the wheel did not turn and was dragged along the surface. More contact forces will be required in these situations to ensure the turning of the wheel. If the wheel does not roll for a few seconds, this is not a problem for the potential measurement because there is enough tap water in the textile around the wheel. In addition, it does not pose any difficulties for the locations of contact as this does not rely on odometry data.

3.3.3. Assessment of the resistance measurement wheels on a mortar block

Figure 12 depicts the results of seven flights with the resistance measurement wheels attached to the flying robot's end effector on the mortar block (section 2.5.4). The results of $R_{4p-wheels}$ are shown for a frequency of 5 kHz. The data indicates a rise in resistivity close to the two areas with plastic parts. All measurements were done in the same direction, utilizing the experimentally derived cell constant for converting $R_{4p-wheels}$ to $\rho_{4p-wheels}$.

Near the two locations with plastic pieces, resistivity increased by a factor ranging from 3 to 7. This factor is similar to the measurement where the sensor was kept fixed at each location (section 3.2.3). Due to the basic transformation from time to space used, there was limited positional accuracy, potentially causing discrepancies in the coordinates. Nevertheless, the individual trials show the repeatability of the measurement.

This trial validated the feasibility of capturing electrical resistance measurements during rolling. However, the driving speed must be reduced to low speeds in the order of centimeters per second, and the analysis of the videos shows that no constant velocity could be achieved.
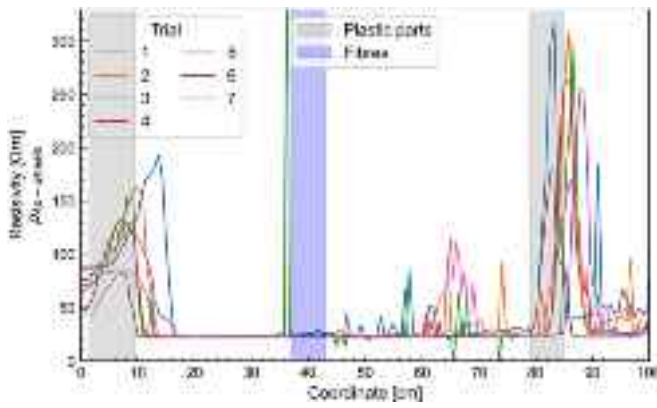
Fig. 12. Results of the resistivity ($\rho_{4p-wheels}$) measurements obtained with the flying robot equipped with the resistance measurement wheels on the reinforced mortar block in seven trials with driving speeds between 0.4 and 0.5 cm/s.

Furthermore, compared to the potential measurements, the driving speed was reduced by a factor of around 5, limiting the acquisition speed of data on engineering structures.

3.3.4. Outdoor flight on a box girder bridge with the point sensor

During an outdoor flight on a box girder bridge, the flying corrosion inspection robot performed an autonomous series of measurements with the point sensor. The flying corrosion inspection robot targeted ten predefined points on the bridge girder capturing HCP values and the electrical resistances ($R_{2p-Sensor}$) (see. Fig. 13).

Figure 14 shows the force (raw data and filtered) and potential readings over the measurement time. The first 30 s (-80 to -60 s) were recorded before the take-off of the flying corrosion inspection robot. 60 s (-60–0 s) after take-off, the force sensor was tared (zero measurement at a value of around -3.8 N), and the time was set to zero. Finally, 95 s after take-off (15 s), the end effector made contact with the bridge girder, and the ten measurements points were approached successively (number of contact points 1–10).

The average time to measure the potential 40 times and to measure three times $R_{2p-Sensor}$ was 9.75 s. In most cases, the rate of measurement acquisition was constant. However, the acquisition rate of the NDT measurements could be reduced by prioritizing the process controlled by ROS to ensure a stable flight (Fig. 15). A filter automatically rejected potentials above 300 mV vs. CSE and below -1500 mV vs. CSE. The filtered data showed that the potentials were constant over time during the contact.

For the first measurement point, the mean contact force was approximately -5.8 N, accounting for the static offset The static offset (zero measurement) was determined in nearly horizontal orientation of the sensor, whereas the measurements on the wall were slightly tilted upwards. The noise in the signal resulted from the vibrations and the slight movement of the flying robot in the air due to wind or self-induced disturbances close to the wall. Furthermore, the orientation of the sensor affects the force measurements results. The absolute value of the contact force was slightly increased after the first contact to ensure reliable physical contact over time for the HCP measurement. No clear correlation could be found between potentials and the applied contact force.

Figure 15 shows the force values and the potentials over time for the first measurement point. The green background colour marks areas where the mean contact force is above the force offset, and the red background indicates forces lower than the force offset. The robot could exert nearly a constant force on the structure during physical contact with the structure. The first 6.5 s of the contact time were used to obtain the potential values, and the other 5.5 s in contact were used to determine the electrical resistance. Fewer potential values were stored at this location compared to the other nine measurements, because of the priority of the data acquisition process in ROS, which delayed the measurement process. The filtered force signal dropped three times below the threshold, but only once the force was insufficient to obtain potential values. In the two latter cases, the robot was able to establish higher forces in a fraction of a second.

Figure 16 shows the planned and executed contact points of the sensor on the bridge. The average deviation from the target point to the impact point of the tip of the sensor was 7.8 cm, with a standard deviation of 2.1 cm. Deviations in the z-direction, which points into the structure, were neglected as they were considered negligible. In eight out of ten points, contact with the structure was established above the target coordinates. This indicates that the end effector of the robot tended to lean upwards while establishing contact with the surface. The deviation from the planned contact point is not a problem for the determination of the corroding areas, especially since the coordinates of the contact point have been accurately verified. Compared to the

Fig. 13. The flying robot with the point sensor mounted on the end effector during a contact perpendicular to the girder with cables going downwards to the Keithley 2000 and the peristaltic pump, the orange reflector for the Total station for state estimation, and the security rope from the top.
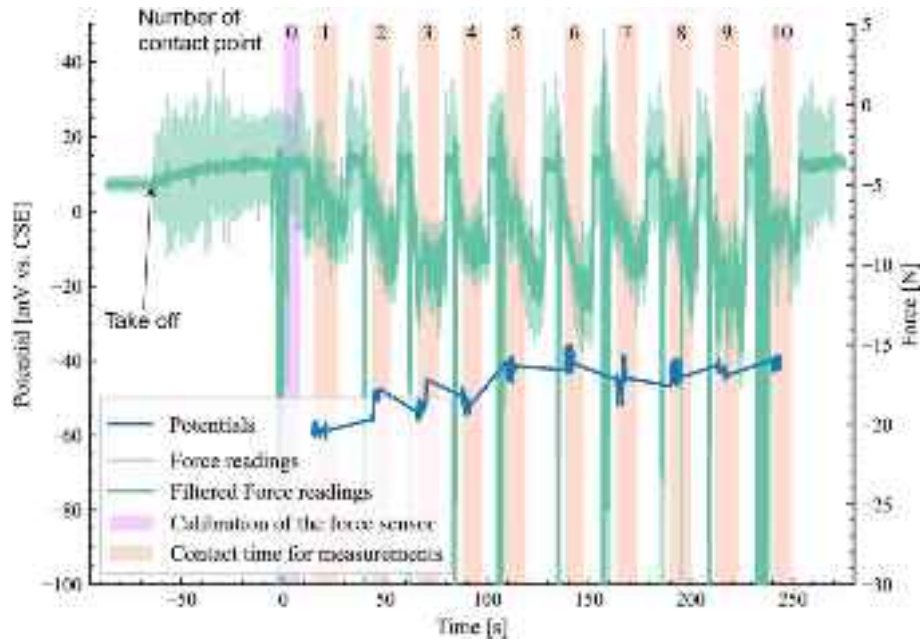
Fig. 14. Potentials and force readings over time during the outdoor flight on the bridge where 10 points were measured in a grid pattern obtained with the flying robot equipped with the point sensor.
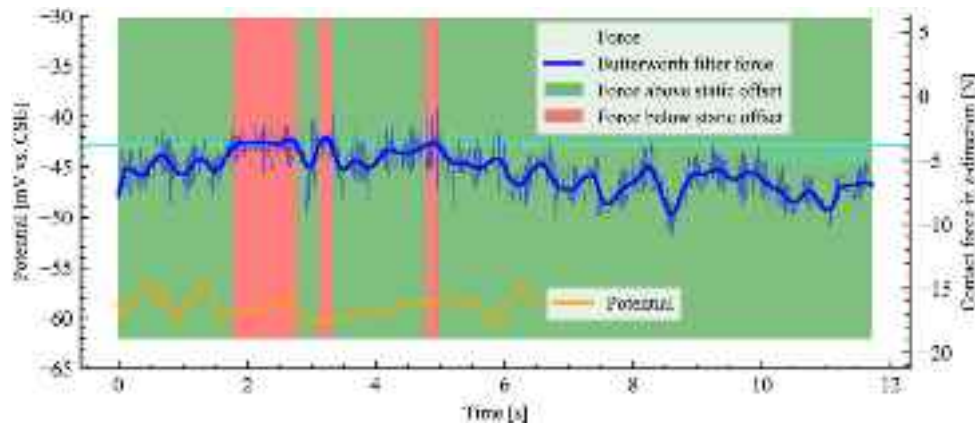

Fig. 15. Force (raw and Butterworth filtered data) and potential against time for the first measured point on the bridge while the sensor was in contact with the concrete surface obtained during a flight. The force reading was below the static offset for certain times but still high enough for a reliable potential measurement.

experiments under laboratory conditions and using external state estimation, the deviation between the executed and planned trajectory is larger, as expected before conducting the experiment.

The conversion of the $R_{2p-Sensor}$ into $\rho_{2p-Sensor}$ was performed using eq. (1) considering a diameter of 15 mm for the tip of the sensor. The average resistivity, based on five measurements per location, ranged between 2.1 and 26.4 k̇m but in the same order of magnitude compared to the experiments in the laboratory. Those values are in accordance with typical values of a 60 year old ordinary Portland cement (CEM I) in a sheltered environment [42]. The $R_{sensor-inner}$ was determined in the laboratory and ranged between 5 and 10 kΩ. For the data correction, the inner resistance was fixed to 10 kΩ. $R_{2p-Sensor}$ was one magnitude higher than $R_{sensor-inner}$. For significantly higher moisture contents, the correction might be more important.

Table 4 presents a detailed overview of the HCP results by presenting the mean potential per location, the standard deviation, and the number of points per measurement taken on the web of the box-girder bridge. The potentials were in a small potential range, ranging from −35 mV vs. CSE to −60 mV vs. CSE and considerably higher compared to the measurements in the laboratory. With a standard deviation under 5 mV, the filter discarded no more than three measurements per point. This suggested that the contact with the concrete surface was sufficient, and the continuous wetting of the sponge ensured sufficient electrolytic contact. The potential values were at a level corresponding to that of passive reinforcement steel [42].

Figure 17 presents a summary of the measurement on the box girder bridge in the 3D scan of the bridge by the total station, including the target points, the actual contact point colored with the median potential, and the recording sequence to minimize the flight distance according to predefined constraints. This data representation shows the potential of combining all available information from inspections that could be further enhanced by using a reference point to align all measurements taken on the same structure. This illustration can include previous or coming condition assessments.

At present, it takes approximately 25 s to acquire one data point. This time included approaching the surface and measuring potentials and electrical resistances. If a complete bridge is to be mapped, the time between points and data capture time becomes significant. With the
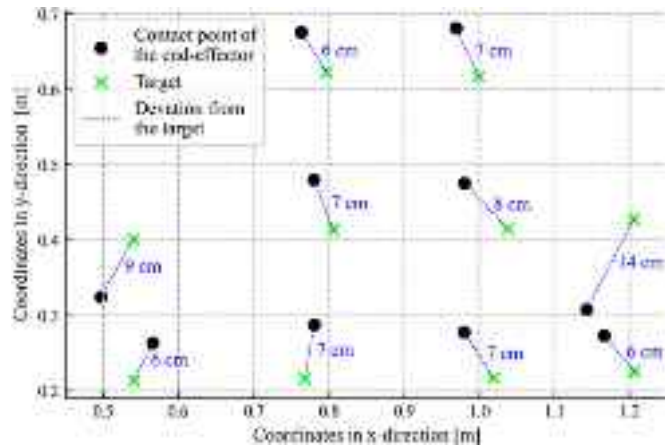
Fig. 16. Aligned frame with the side of the box girder bridge at the underside, where the desired location of the contact point with the sensor on the surface is shown in comparison with the actual contact point with the deviation.

current speed, it would take approximately 14 h to measure 2000 points at 25 s per point. The 2000 points would be equal to approximately 250 m^2 of concrete surface measuring in a grid of 25 cm × 25 cm. This outdoor flight demonstrated the feasibility of taking measurements autonomously on a structure outside the laboratory environment with sufficient spatial accuracy for the task. No optimization of the speed and acceleration of the flying platform was performed, and the distance to the surface was kept larger than necessary for safety reasons. Since reliable potentials were recorded shortly after contact, the number of recorded potentials per measuring point could be significantly reduced for further measurements. Alternatively, a method of reducing the time in contact with the structure is to define a criterion for the stability of the

potential.

4. Conclusions and outlook

This paper described the development and validation of two sensors tailored to acquire contact-based NDT data (HCP and electrical concrete resistivity) autonomously and with the help of a flying inspection robot on RC. The versatility of the robotic platform allowed for taking measurements on concrete surfaces with different orientations. The functionality of the sensors was presented in comparisons between manual measurements and measurements taken with the robot. The following major conclusions are drawn:

1) A "point sensor" was developed that allows the combined measurement of HCP and concrete resistivity, the latter with a two-point measurement (between the probe and the reinforcement, $\rho_{2p-Sensor}$). A major novelty of the point sensor was an approach that allowed monitoring the functionality of the probe. This was achieved by a system to measure the probe's internal electrical resistance ($R_{sensor-inner}$), which allows detecting any loss of electrical contact to the structure, e.g., due to probe drying. This "self-checking" feature of the probe is considered a major advantage for autonomous measurements, where a human operator may not be present to continuously check and ensure the probe's functionality.
2) A probe consisting of five wheel-electrodes was developed that allows the combined measurement of HCP and concrete resistivity, the latter by a four-point measurement ($\rho_{4p-wheels}$). The main advantage of this wheel-electrode-based probe is the faster data acquisition; while the surface can be scanned at a rate of up to cm/s, the data acquisition with the "point sensor" is slower.
3) Both the "point sensor" and the probe containing 5 wheel-electrodes were validated against manual measurements and each other. The good agreement found between the different measurements suggests

Table 4
Overview of the results from the HCP measurement on the wall with the mean potential, the standard deviation, and the number of points per measurement location after filtering.

	Point number									
	1	2	3	4	5	6	7	8	9	10
Mean potential [mV vs. CSE]	−58	−51	−52	−51	−42	−40	−45	−43	−43	−40
Standard deviation [mV vs. CSE]	1.2	3.0	2.6	1.7	1.9	2.2	3.4	1.9	1.1	1.1
Number of potential values	37	40	39	40	40	40	39	39	38	40
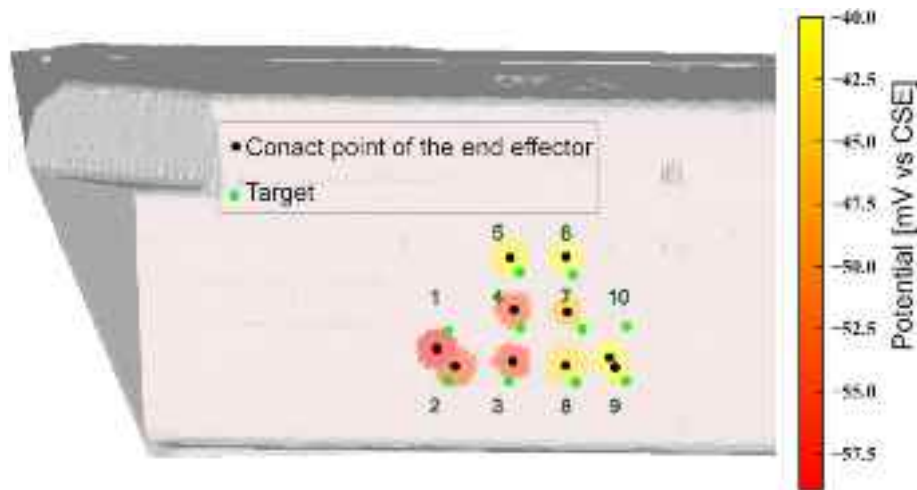
Fig. 17. 3D scan of the bridge surface overlaid with the mean values of the recorded potential. The planned points are shown in green, and the estimated contact points by the robot arm are shown in black circles. The blue numbers indicate the recording sequence obtained on the box girder bridge. (For interpretation of the references to colour in this figure legend, the reader is referred to the web version of this article.)

that the developed probes are feasible for implementation in auto-mated inspection devices, such as flying robots.

4) Different strategies were presented in this work to ensure probe functionality during operation as well as detect loss of contact be-tween probe and structure (e.g., electrical resistance measurements, data filtering). Such features are considered crucial for autonomous, contact-based NDT inspection technologies. While the approaches presented here proved effective, further developments may optimize the robustness of the sensor against mechanical damage, reduce the measurement time, and thus improve the efficiency of data acquisition.

The need for efficient, spatially referenced condition assessment is expected to grow with the continuous aging of the infrastructure, particularly on hardly accessible parts. Non-destructive corrosion detection offers the advantage of locating damage at an early stage, thus potentially leading to cost-effective repairs and prolonging the expected service life. This advantage could make the initial investment in such technology worthwhile. Additionally, robotic contact-based assessment of assets is being developed in various industries. These developments will contribute to a decrease in costs while increasing the capabilities of the commercially available flying robots at the same time. This expected development will improve the data collection quality and repeatability of the NDT assessment of RC structures in the long term, surpassing the traditional approach in the long term.

Overall, developments in the area of contact-based NDT probes compatible with robots, such as flying or climbing robots, will contribute to automating inspection and condition assessment of civil engineering structures in the future. However, despite the technological challenges, legal aspects must be covered in order to allow such in-spections in the future.

Supplementary data to this article can be found online at https://doi.org/10.1016/j.autcon.2023.105241.

CRediT authorship contribution statement

P. Pfändler: Writing – original draft, Visualization, Methodology, Investigation, Formal analysis, Conceptualization. **K. Bodie:** Writing – review & editing, Methodology, Investigation, Conceptualization. **G. Crotta:** Writing – review & editing, Methodology, Investigation, Conceptualization. **M. Pantic:** Writing – review & editing, Visualization, Methodology, Conceptualization. **R. Siegwart:** Writing – review & editing, Supervision, Funding acquisition. **U. Angst:** Writing – original draft, Supervision, Funding acquisition, Conceptualization.

Declaration of Competing Interest

The authors declare that they have no known competing financial interests or personal relationships that could have appeared to influence the work reported in this paper.

Data availability

Data will be made available on request.

References

[1] R.J. Flatt, N. Roussel, C.R. Cheeseman, Concrete: an eco material that needs to be improved, J. Eur. Ceram. Soc. 32 (2012) 2787–2798, https://doi.org/10.1016/j.jeurceramsoc.2011.11.012.

[2] D. Yilmaz, U. Angst, Korrosionsbedingte Kosten an Ingenieurbauwerken im Schweizer Straßennetz, Beton- Stahlbetonbau. 115 (2020) 448–458, https://doi.org/10.1002/best.202000004.

[3] A.E.K. Jones, Development of an Holistic Approach to Ensure the Durability of New Concrete Construction, ISBN: 9780721015224, British Cement Association, Crowthorne, 1997.

[4] R.B. Polder, W.H.A. Peelen, W.M.G. Courage, Non-traditional assessment and maintenance methods for aging concrete structures - technical and non-technical issues, in: Materials and Corrosion, John Wiley & Sons, Ltd, 2012, pp. 1147–1153, https://doi.org/10.1002/maco.201206725.

[5] U. Angst, B. Elsener, A. Jamali, B. Adey, Concrete cover cracking owing to reinforcement corrosion - theoretical considerations and practical experience, Mater. Corros. 63 (2012) 1069–1077, https://doi.org/10.1002/maco.201206669.

[6] R.J. Woodward, F.W. Williams, Collapse of Ynys-y-Gwas bridge, West Glamorgan, in: Proc. Inst. Civ. Eng, 1988, pp. 635–669, https://doi.org/10.1680/iicep.1988.179.

[7] R.J. Woodward, Collapse of a segmental post-tensioned concrete bridge, Transp. Res. Rec. (1989) 38–59. ISBN: 0309048087.

[8] D. Breysse, Nondestructive evaluation of concrete strength: an historical review and a new perspective by combining NDT methods, Constr. Build. Mater. 33 (2012) 139–163, https://doi.org/10.1016/J.CONBUILDMAT.2011.12.103.

[9] F. Akgul, Inspection and evaluation of a network of concrete bridges based on multiple NDT techniques, Struct. Infrastruct. Eng. 17 (2020) 106–1095, https://doi.org/10.1080/15732479.2020.1790016.

[10] Schweizerischer Ingenieur- und Architektenverein, Planung, Durchführung und Interpretation der Potenzialmessung an Stahlbetonbauten, 2013, pp. 1–40 (Last access: 7.11.2023).

[11] R. Polder, R. Weydert, M. Raupach, RILEM TC 154-EMC: electrochemical techniques for measuring metallic corrosion: test methods for on site measurement of resistivity of concrete, Mater. Struct. = Matér. Construct. 33 (2000) 603–611, https://doi.org/10.1617/13952.

[12] C. Sodeikat, Merkblatt B3 - Elektrochemische Potentialmessungen zur Detektion von Bewehrungsstahlkorrosion Veröffentlicht vom DGZfP-Fachausschuss für Zerstörungsfreie Prüfung im Bauwesen - Unterausschuss Korrosionsnachweis für Stahlbeton, Beton- Stahlbetonbau. 105 (2010) 529–538, https://doi.org/10.1002/best.201000043.

[13] T.F. Mayer, A. Burkert, G. Ebell, T. Eichler, K. Hariri, J. Harnisch, S. Keßler, J. Mietz, K. Reichling, C. Sodeikat, Specification B 03 Electrochemical Half-Cell Potential Measurements for the Detection of Reinforcement Corrosion, 2014 (Last access 28.10.2021).

[14] ASTM, C876-15, ASTM standard C876, Annual Book of ASTM Standards, 2015, pp. 1–8, https://doi.org/10.1520/C0876-15.2. (Last access 29.09.2020).

[15] U. Angst, P. Pfändler, F. Martinelli Orlando, M. van Ede, L. Michel, Corrosion for Civil Engineers Part 4: Potential Measurement to Detect Corrosion of Steel in Concrete - YouTube. https://www.youtube.com/watch?v=jyforfSMAis&ab_channel=ETHCorrosion, 2020.

[16] B.B. Kocer, T. Tjahjowidodo, M. Pratama, G.G.L. Seet, Inspection-while-flying: an autonomous contact-based nondestructive test using UAV-tools, Autom. Constr. 106 (2019), https://doi.org/10.1016/J.AUTCON.2019.102895.

[17] D. Lattanzi, G. Miller, Review of robotic infrastructure inspection systems, J. Infrastruct. Syst. 23 (2017) 1–16, https://doi.org/10.1061/(asce)is.1943-555x.0000353.

[18] T. Rakha, A. Gorodetsky, Review of unmanned aerial system (UAS) applications in the built environment: towards automated building inspection procedures using drones, Autom. Constr. 93 (2018) 252–264, https://doi.org/10.1016/J.AUTCON.2018.05.002.

[19] H. Bonyan Khamseh, F. Janabi-Sharifi, A. Abdessameud, Aerial manipulation—A literature survey, Robot. Auton. Syst. 107 (2018) 221–235, https://doi.org/10.1016/j.robot.2018.06.012.

[20] F. Ruggiero, V. Lippiello, A. Ollero, Aerial manipulation: a literature review, IEEE Robot Autom Lett. 3 (2018) 1957–1964, https://doi.org/10.1109/LRA.2018.2808541.

[21] R. Moryson, H.G. Herrmann, BetoScan 2.0 – Werkzeug für die proaktive Lebenszyklusbetrachtung, Bautechnik. 94 (2017) 730–735, https://doi.org/10.1002/BATE.201700069.

[22] N. Gucunski, S.H. Kee, H. La, B. Basily, A. Maher, H. Ghasemi, Implementation of a fully autonomous platform for assessment of concrete bridge decks RABIT, in: Structures Congress 2015 - Proceedings of the 2015 Structures Congress, 2015, pp. 367–378, https://doi.org/10.1061/9780784479117.032.

[23] A. Leibbrandt, G. Caprari, U. Angst, R.Y. Siegwart, R.J. Flatt, B. Elsener, Climbing robot for corrosion monitoring of reinforced concrete structures, in: 2012 2nd International Conference on Applied Robotics for the Power Industry, CARPI 2012, IEEE Computer Society, 2012, pp. 10–15, https://doi.org/10.1109/CARPI.2012.6473365.

[24] A. Akutsu, E. Sasaki, K. Takeya, Y. Kobayashi, K. Suzuki, H. Tamura, A comprehensive study on development of a small-sized self-propelled robot for

bridge inspection, Struct. Infrastruct. Eng 13 (2016) 1056–1067, https://doi.org/10.1080/15732479.2016.1236132.

[25] B. Li, K. Ushiroda, L. Yang, Q. Song, J. Xiao, Wall-climbing robot for non-destructive evaluation using impact-echo and metric learning SVM, Int. J. Intell. Robot. Appl. 1 (2017) 255–270, https://doi.org/10.1007/S41315-017-0028-4.

[26] G. Gallegos Garrido, T. Pervez Sattar, An Autonomous Wall-Climbing Robot for Inspection of Reinforced Concrete Structures: SIRCAUR, Artificial Intelligence and Technology, Special Issue on Mobile Service Robotics and Associated Technologies, 2021, pp. 188–196, https://doi.org/10.37965/jait.2021.0016.

[27] J. Wells, B. Lovelace, Unmanned Aircraft System Bridge Inspection Demonstration Project Phase II Final Report. https://transportation.org/uas-aam/wp-content/uploads/sites/80/2023/05/201718.pdf, 2017 (accessed March 20, 2021).

[28] S. Sankarasrinivasan, E. Balasubramanian, K. Karthik, U. Chandrasekar, R. Gupta, Health monitoring of civil structures with integrated UAV and image processing system, in: Procedia Comput Sci, Elsevier, 2015, pp. 508–515, https://doi.org/10.1016/j.procs.2015.06.058.

[29] S. Sony, K. Dunphy, A. Sadhu, M. Capretz, A systematic review of convolutional neural network-based structural condition assessment techniques, Eng. Struct. 226 (2021), 111347, https://doi.org/10.1016/j.engstruct.2020.111347.

[30] K. Bodie, M. Brunner, M. Pantic, P. Pfändler, R. Siegwart, J. Nieto, U.M. Angst, An Omnidirectional Aerial Manipulator for Contact-Based Inspection, in: Robotics: Science and Systems, 2019, pp. 1–9, https://doi.org/10.15607/RSS.2019.XV.019.

[31] K. Bodie, Z. Taylor, M. Kamel, R. Siegwart, Towards efficient full pose Omnidirectionality with Overactuated MAVs, in: J. Xiao, T. Kröger, O. Khatib (Eds.), Proceedings of the 2018 International Symposium on Experimental Robotics, Springer International Publishing, Cham, 2020, pp. 85–95, https://doi.org/10.1007/978-3-030-33950-0_8.

[32] K. Bodie, M. Brunner, M. Pantic, S. Walser, P. Pfändler, U. Angst, R. Siegwart, J. Nieto, Active interaction force control for contact-based inspection with a fully actuated aerial vehicle, IEEE Trans. Robot. 37 (2021) 709–722, https://doi.org/10.1109/TRO.2020.3036623.

[33] P. Pfändler, K. Bodie, U. Angst, R. Siegwart, Flying corrosion inspection robot for corrosion monitoring of civil structures – First results, in: SMAR 2019 - Fifth Conference on Smart Monitoring, Assessment and Rehabilitation of Civil Structures, 2019, pp. 1–8, https://doi.org/10.3929/ETHZ-B-000365572.

[34] S. Feliu, C. Andrade, J.A. González, C. Alonso, A new method for in-situ measurement of electrical resistivity of reinforced concrete, materials and structures/Materiaux et, Constructions. 29 (1996) 362–365, https://doi.org/10.1007/bf02486344.

[35] U.M. Angst, B. Elsener, On the applicability of the wenner method for resistivity measurements of concrete, ACI Mater. J. 111 (2014) 661–672, https://doi.org/10.14359/51686831.

[36] L. Bertolini, B. Elsener, E. Redaelli, R. Polder, Corrosion of Steel in Concrete: Prevention, Diagnosis, Repair: Second Edition, Corrosion of Steel in Concrete: Prevention, Diagnosis, Repair, Second edition, 2013, https://doi.org/10.1002/9783527651696. ISBN 978-3527331468.

[37] R. Polder, C. Andrade, B. Elsener, Ø. Vennesland, J. Gulikers, R. Weidert, M. Raupach, Test methods for on site measurement of resistivity of concrete, Mater. Struct. 33 (2000) 603–611, https://doi.org/10.1007/bf02480599.

[38] S.G. Millard, Reinforced concrete resistivity measurement techniques, Instit. Civ. Eng. Proc. 91 (1991) 71–88, https://www.icevirtuallibrary.com/doi/pdf/10.1680/iicep.1991.13583 (accessed January 31, 2023).

[39] R. Vonäsch, R. Knuser, German: Modellprobekörper für Potentialmessungen - Herstellung und Simulation (Mock-ups for half-cell potential measurements: production and simulation), ETH Zürich p. 1-32(2013) (Last access: 03.09.2020).

[40] F. Presuel-Moreno, Y. Liu, Y.Y. Wu, Numerical modeling of the effects of rebar presence and/or multilayered concrete resistivity on the apparent resistivity measured via the Wenner method, Constr. Build. Mater. 48 (2013) 16–25, https://doi.org/10.1016/j.conbuildmat.2013.06.053.

[41] P. Azarsa, R. Gupta, Electrical resistivity of concrete for durability evaluation: a review, Adv. Mater. Sci. Eng. 2017 (2017) 1–30, https://doi.org/10.1155/2017/8453095.

[42] L. Bertolini, B. Elsener, P. Pedeferri, R.B. Polder, Corrosion of Steel in Concrete, Wiley, 2003, https://doi.org/10.1002/3527603379. Online ISBN: 9783527603374.

[43] J. Sanchez Carmen Andrade Julio Torres Nuria Rebolledo Jose Fullea, Determination of reinforced concrete durability with on-site resistivity measurements, Mater. Struct. 50 (2017) 1–9, https://doi.org/10.1617/s11527-016-0884-7.

[44] B. Elsener, C. Andrade, J. Gulikers, R. Polder, M. Raupach, Half-cell potential measurements-potential mapping on reinforced concrete structures, Mater. Struct. 36 (2003) 461–471, https://doi.org/10.1007/BF02481526.